WILEY | Hindawi

Research Article

Application of Fiber Grating Sensing in Similar Model Impact Tests of Underground Engineering

Lei Gao,[1,2] **Zhihao Li** [ORCID],[2] **Jie Li,**[1,2] **Zhen Wang,**[1] **Haiming Jiang,**[2] **and Mingyang Wang**[1,2]

[1]*College of Mechanical Engineering, Nanjing University of Science and Technology, Nanjing 210094, China*
[2]*State Key Laboratory of Explosion and Impact and Disaster Prevention and Mitigation, Army Engineering University of PLA, Nanjing, Jiangsu 210007, China*

Correspondence should be addressed to Zhihao Li; 17865191593@163.com

To clarify damage or degradation mechanisms of underground shock disturbance of deep caverns, a customized model of a deep cavern to subjected ground shock was employed to simulate the following properties and processes: crustal stress loading, cavern excavation, and ground-shock disturbance loading. The similar model specimen was a cube of 1.3 m length and a size similarity ratio of 1 : 50. A fiber Bragg grating (FBG) strain sensor with multipoint distributions was developed to monitor the distribution of internal strains in the model. Sensors were appropriately arranged and packaged in the similar model of deep rock to determine strain variation in the model under hydrostatic confining pressure, construction dynamic load, and shock dynamic load. This investigation involved high crustal stress simulation, tunnel boring machine (TBM) construction simulation, and deep explosive shock simulation, respectively. The results suggest that the sensors can accurately monitor the strain during the entire process comprising loading, excavation, and shock generation and obtain the distribution of cave strain during excavation and shock generation. The cave strain indicated that the left and right sides of the tunnel both experienced a rapid increase in tensile strain from the top plane shock wave, proportional to the shock force. The mechanism of surrounding rock failure and the occurrence of the V-shaped blasting pit were clarified. In the model test, the following phenomena related to deep tunnel failure were simulated: particle ejection, block collapse, slabbing, and tunnel face collapse. The oscillatory wave was also monitored with FBG sensors. The results demonstrated that FBG strain sensor had good repeatability and could accurately monitor strain change in the different blocks, thus demonstrating considerable potential for use in similar model tests. The model tests conducted in this study can provide important technical reference and support for the construction and protective design of deep caverns.

1. Introduction

In deep underground engineering, rock mass strength is significantly affected by the existence of water, cracks, and holes. Simulating the influence of water and various holes on rock mass strength is challenging in a theoretical study. However, relying on similarity theory which is applied in many fields of natural and engineering science, the similarity model test has become an important means of studying the stability of underground engineered structures under complex geological conditions such as water-sensitive strata and fissure faults. In 1936, following the similarity theory [1], Manchao and Qihu conducted a similar model test by substituting bedrock with artificial material in the following manner. A plane model with a 100 : 1 scale similarity ratio was constructed to simulate constructions at depths of 300–2500 m. Its main use was the clarification of rock deformation and failure, but in addition, this method can be effectively combined with theoretical analysis and calculation to simplify the study subject and approximate real conditions. The Kuznetsov test pioneered engineering geomechanical model testing. Similar studies have been reported globally [2–6], and geomechanical model tests have become a key research measure in geotechnical and mineral engineering. Indeed, the mechanical study of deep rock subjected to vibrational shock still requires further improvement, with the methodology and experimental platforms still at the exploratory

stages. Experimental platforms and apparatus suitable for deep rock are currently being developed [7–12]; therefore, research is likely to focus on the innovative application of traditional measuring technologies and the introduction of new sensing technologies for the dynamic response of deep rock. Such a new sensing technology is the fiber grating sensing.

The parameters measured in geomechanical model tests include stress, strain, displacement, fracture, and failure. Many test instruments used for the measurement of stress, strain, and displacement in rock engineering are sometimes unsuitable because they are large, have single point measurement, and are difficult to place in the model, thus necessitating the development of special test instruments or test approaches. In geomechanical model tests of stress and strain, traditional electrical measurement methods such as resistance strain gauge and pressure gauge are usually adopted.

Strain gauge technology is advanced; its performance is stable; its accuracy and sensitivity are high; its range is large, and it has wide economic applicability. In deep-ground geomechanical model tests, the resistance strain gauge is easily affected by the external environment and its anti-electromagnetic interference ability is poor. Additionally, each strain gauge leads two wires from the model, which affects the model's integrity and can damage the model when a large number of sensors are buried in it. In model tests, pressure sensors tend to be too large, the lateral stiffness is too small, and the sensor material may be incompatible with the material of the model. Embedded sensors have an impact on stress distribution and variation in the model, so there is often a difference between the measured results and the practical value. The sensors are also affected by environmental changes; that is, they are vulnerable to zero drift [13].

A better alternative is fiber strain sensing. Fiber strain sensing can achieve long-distance real-time monitoring and transmission on account of its high sensitivity, small size, strong anti-interference ability, distributed measurement, and several other advantages. Therefore, it is gradually becoming a preferred method of monitoring stress and strain in geomechanical models. Mendez et al. [14] were the first researchers to apply fiber sensing to internal monitoring in medium. At present, fiber sensing methods commonly used in model testing include fiber Bragg grating sensing (FBG), optical time-domain reflection (OTDR), and Brillouin optical time-domain analyzer and Brillouin optical time-domain reflectometry (BOTDA and BOTDR) [15–22]. Of these methods, grating sensors are widely used in machine tool processing, construction of roads and bridges, and other industries. Grating sensors have the advantage of easy digital implementation, high accuracy (up to nanoscale), excellent interference resistance, easy installation, and good reliability. Since it is fully digitized, there are no manual reading errors [23–25]. Additionally, grating sensors provide a good technical means for monitoring stress and strain in geomechanical models on account of distributed measurement, real-time monitoring, and long-distance data transmission.

Several researchers have utilized fiber sensing in their work. Li and Wang [26] applied fiber measurement technology in the geomechanical model tests of Xiluodu underground workshop, and Yang et al. [27] applied fiber grating sensing in a geomechanical model test of an arch dam. Wu et al. [28]

used similar packaging materials to encapsulate coated grating to create a model, to which he attached a fiber sensor, based on which the strain transfer law of the interior of the material was investigated. Wang et al. [29] devised a fiber grating bolt sensor by combining an aluminum rod, fiber grating, and fiber grating strain sensor, to conduct the real-time monitoring of strain of a model in the simulation of a landslide. Three-dimensional fiber grating for similar materials has been designed and applied in different geomechanical tunnel model tests [30–32], and numerical simulation is used to study the mechanical characteristics of the sensor.

There have been several studies applying fiber grating sensing to the measurement of internal strain of similar materials, as well as the analysis of the strain transfer law of grating and fiber embedded in similar materials [33–35]. Gu and Yuan [36] designed a new fiber grating sensor layout process to investigate the stress and strain evolution of overburden failure in a coal seam; the mine pressure and displacement in front of the working face were monitored in a simulated mining process using a geological model. The monitoring results and model test results were consistent with engineering practice, thus providing a new method for separation discrimination in engineering practice. To improve the accuracy of FBG strain sensor measurement in static pressure model tests on pipe piles, Wang et al. [37] proposed a calibration method to determine the theoretical sensitivity coefficient of the fiber grating sensor and experimental sensitivity coefficient of strain. The test results of the calibrated FBG strain sensor were highly accurate, thus laying a foundation for the monitoring technology for model pipe-pile tests using the FBG strain sensor.

Test applications of fiber sensing technology have been conducted in static load and low-frequency vibration simulation in geomechanical model tests. Excellent results have been obtained in sensor design, encapsulation and embedding, and the strain transfer law of model materials. However, the application of fiber sensing technology in shock simulation tests in deep rock needs further investigation. Currently, deep rock similar model test apparatuses are still in development and constantly being improved. For example, independently developed test devices are being used to simulate the dynamic response of deep rock to high crustal stress, tunnel excavation, and explosive ground shock.

This study focuses on strain testing of similar material models in the simulation of these three properties/processes: high crustal stress, tunnel excavation, and explosive ground shock. On the basis of the analysis of the characteristics of similar model experiments and the principles of grating sensing, an appropriate quasidistributed grating string sensor was designed, and a calibration test on a beam of constant strength and a similar model specimen was carried out, which provided a way to determine its applicability. In addition, a sensor was placed inside a similar model of deep rock using an appropriate layout process and packaging method. The following investigations were conducted: high crustal stress simulation to determine strain variations in the model under hydrostatic confining pressure, TBM construction simulation to determine construction dynamic load, and deep explosive shock simulation to determine shock dynamic load. The results

TABLE 1: Similarity ratio values.

Parameters	Unit	Ratio of similitude	Relations	Reduced scale
Density	kg/m^3	C_ρ	$C_\rho = 1$	1
Size	m	C_L	C_L	50
Peak stress	MPa	C_{P_f}	$C_{P_f} = C_\rho C_L$	50
Compressive strength	MPa	C_σ	$C_\sigma = C_\rho C_L$	50
Tensile strength	MPa	C_σ	$C_\sigma = C_\rho C_L$	50
Modulus of elasticity	MPa	C_E	$C_E = C_\rho C_L$	50
Poisson's ratio	/	C_μ	$C_\mu = C_\varepsilon$	1
Time	s	C_t	$C_t = \sqrt{C_L}$	7.07
Speed	m/s	C_v	$C_v = \sqrt{C_L}/C_\rho$	7.07
Strain		C_ε	$C_\varepsilon = C_L/C_L$	1

provide reliable experimental data for the verification of several mechanical phenomena and theoretical studies of deep rock in similar model tests.

2. Experiments

2.1. Experimental Design. During large-scale explosions, stress waves propagate from the explosion center, during which the wave front expands and the positive pressure time increases. When a cavern is sufficiently far away from the explosion center and the radius of the stress wave is large enough, the stress wave can be simplified into a long-term loaded plane wave.

To simulate the failure process of a deep cavern under the action of a far-field large explosion or far-field earthquake and to obtain the failure mechanism of deep caverns under the action of plane wave dynamic disturbance, this study involved a similar model test. In the test, the size similarity ratio of prototype and model was set as 50 : 1 and the density similarity ratio was 1 : 1. The similarity ratios of all parameters were calculated according to the similarity principle, which are shown in Table 1.

The depth of the cavern was assumed to be 300 m. The size of the vertical crustal stress was calculated according to the gravity of the upper rock, and the horizontal crustal stress and vertical crustal stress were assumed to be the same. Then, the crustal stress can be determined with the following formula [38].

$$\sigma_h = \gamma H, \tag{1}$$

where γ is the unit weight of rock, which equals the similar materials density in this study, i.e., 2540 kg/m^3.

The confining pressure required for the model test was 0.16 MPa according to the 50 : 1 stress similarity ratio.

The actual closed explosive yield was taken as 10–100 kt, under the effect of $(100 - 1500)Q^{1/3}$, and the peak pressure

falls within a certain range [39].

$$p_f = \rho C_p A \left(\frac{r}{Q^{1/3}} \right)^{-n} \approx (2 \sim 145)\text{MPa}, \tag{2}$$

where ρ is the rock density (2500–2700 kg/m^3), C_p is the longitudinal wave velocity (4000–6000 m/s), r is the distance from the explosion center (unit: m), and A and n are the empirical coefficients obtained from the field test ($A = 8.94 \times 10^4$ and $n = 2.21$ for dry hard rock).

The plane shock-stress peak for the model test was 0–3 MPa according to the 50 : 1 stress similarity ratio.

2.2. Deep-Rock Model Test Set-Up. A customized deep-cavern ground-shock disturbance loading system was adopted to conduct the similar model test. Figure 1 shows the general framework of the proposed testing system. It comprises the fundamental platform, the crustal stress loading simulation system, the excavation disturbance simulation system, and the explosive disturbance loading simulation system. The device can provide uniform static loading, excavation simulation, and dynamic loading of explosive shock [40].

The crustal stress loading simulation system was used to simulate the initial mechanical environment of deep rock; the system was capable of stable long-term static loading for the model specimen. In order to ensure model stability during loading, the model specimen was passively loaded at the bottom, and active loading was applied in five other directions. Different levels of static load were applied to the different boundaries of the model specimen to achieve true triaxial loading on the model.

The computer-controlled excavation disturbance simulation system executed the excavation of a circular cavern. The maximum excavation diameter and depth were 200 mm and 1 m, respectively. This system comprised a cutter head, a cutter handle, a reducer, an AC servo motor, and a support stand.

FIGURE 1: Deep-cavern ground-shock disturbance loading system.

The function of the explosive disturbance loading simulation system was to generate dynamic load disturbance and apply plane ground-shock disturbance to the top of the model within an area of 1.3×1.3 m. The system consists of an air tank, a solenoid valve, a launch tube, an impact bomb, a plastic capsule, and a piston, which can achieve dynamic pressure loading with a peak capacity of 0–3 MPa.

In summary, when the similarity ratio is within 1 : 50–1 : 100, the main simulation conditions of the test device are to simulate deep underground engineering operations at depths of 0–2000 m and to simulate a ground-shock disturbance induced by the equivalent of a 10–100 kt underground mass explosion.

2.3. Specimen Preparation

2.3.1. Selection of Similar Materials. A 1 : 50 scale similar model test was conducted in this study. The similar model materials are as follows:

(1) Barite sand and quartz sand used as coarse aggregate with a particle size of 0.6–1.18 mm

(2) Barite powder used as fine aggregate with fineness of 300 to 400 mesh

(3) Primary rosin used as a cementing agent

(4) Rubbing alcohol (95% alcohol by volume) used as a blender

Rosin-cemented similar materials were prepared by pressurized molding at 2 MPa pressure. The mold was removed after shaping, and the sample was then demolded and left for natural curing for 5–7 d. MTS microcomputer control electronic pressure testing machine and other test instruments were used to carry out related tests. Table 2 lists the parameters of the similar materials obtained, which are consistent with the similarity ratio of practical rock (50 : 1, the ratio of prototype to model).

2.3.2. Specimen Design and Sensor Arrangement. The specimen was an intact cube 1.3 m in length. Figure 2(a) presents the side view of the specimen. 500 mm of the specimen was used for whole casting. The density was used as a control index for layered casting, each layer with 4 cm high. The detailed process was as now described. The mixed similar materials with specified weight were compressed to form a certain shape and then shaved and sprayed with alcohol after the first layer dried. Then, the second layer was cast. The top 800 mm of the model was divided into parts I–IV from the back to front. Part III was made by piling 10 cm cubic blocks to simulate the block structure of deep rock, while the rest was made by whole casting. The block was made in advance, and fine sand was poured into the spaces between the vertical direct joints of blocks with a controlled width within 2 mm to simulate cracks between blocks. No fine sand was added to the horizontal joint to reduce stress wave decay from top to bottom. During cavern excavation, the excavation was carried out from front to back, i.e., from part IV to parts III and II, with an excavation length of 1 m. Part I was not excavated to ensure back loading uniformity.

The grating sensor and dynamic pressure sensor were placed inside the specimen during the preparation process. Figure 2(b) shows the positions of the blocks for part III and the dynamic pressure sensors (D1-D3) after excavation. Figure 2(c) shows the placement of grating sensors, where the cavern will be formed by later excavation. Of these, A1 to A3 and B1 to B3 were bonded with epoxy resin, while C1 to C3 were bonded with hot melt adhesive. Upon completion of cavern excavation, a microindustrial camera was placed inside the cavern to monitor cavern damage.

2.4. Procedure. The deep-rock model test device works as described hereunder.

2.4.1. Static Loading. Confining pressure was imposed by passive loading of water bags on the five contact surfaces and the bottom to simulate crustal stress on the model. The static loading sequence had a three-way circular loading; the loading amount was controlled at 0.1 MPa each time. After 0.5 MPa, loading was stopped and the pressure was kept constant to accelerate the creep of the specimen. After two days of pressure stabilization, the three-way pressure was lowered to 0.16 MPa to simulate the stress environment at a depth of 300 m. After the internal stress of the specimen became stable, the next phase of the test was conducted. Through this process, the specimen received loading from the surface, and the generated strain gradually changed to stress and transferred to the interior, forming a stable internal stress.

2.4.2. Simulation of Tunnel Excavation. The excavation process was simulated by drill excavation through the reserved

TABLE 2: Mechanical parameters of similar materials.

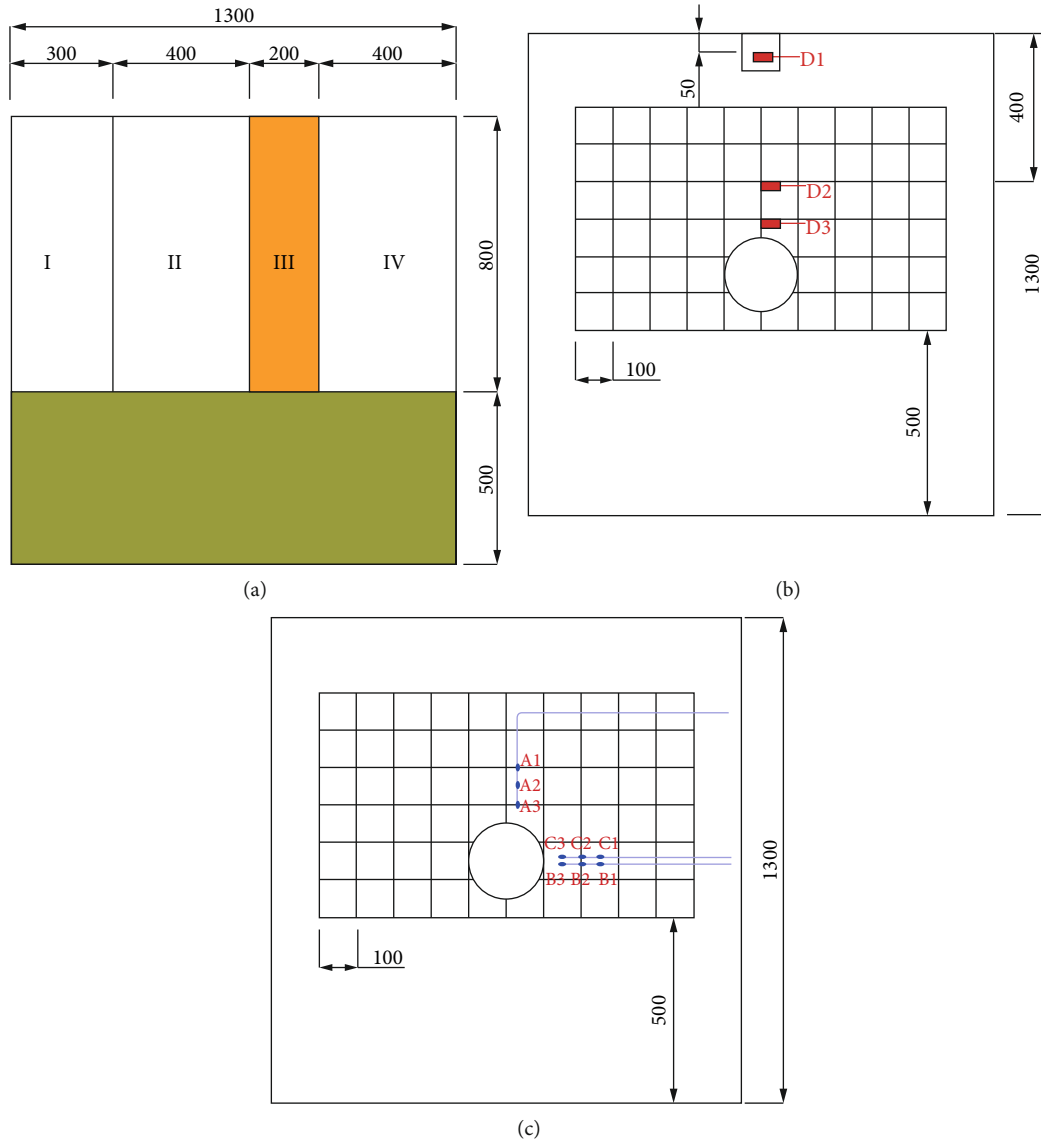| Density (kg/m³)	Elastic modulus (MPa)	Compressive strength (MPa)	Tensile strength (MPa)
2540	441	1.14	0.1

(a)

(b)

(c)

FIGURE 2: Schematic of the similar model (unit: mm): (a) specimen placement; (b) block position and dynamic pressure sensor placement in part III; (c) grating sensor placement in part III.

holes in the front. A deep-tunnel model 20 cm in diameter and 100 cm in length was formed after the simulation. The excavation was performed 10 times, and the excavation length each time was 10 cm.

2.4.3. Simulation of Plane Dynamic Loading Similar to a Far-Field Explosion. A flat shock load was applied to the top of the model, and the occurrence of strain deformation and rock failure of the interior of the model and tunnel was checked. Multiple tests under different shock pressures were performed to study the failure characteristics of a cavern subjected to different shock pressures.

Whether the fiber grating sensor can be used in dynamic strain monitoring in deep rock model testing is dependent on whether effective strain data can be collected at these three stages as described.
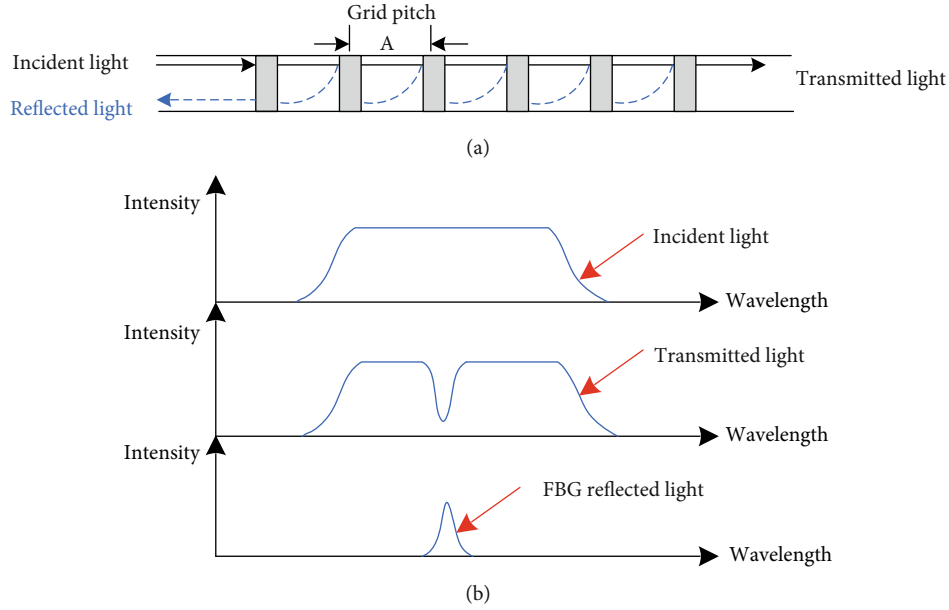
Figure 3: Grating reflection diagram [42]: (a) fiber Bragg grating; (b) reflected light wavelength.

3. Development of Fiber Grating Sensor

In order to measure the strain in key internal positions of the specimen at each stage of the test, appropriate multipoint distributed FBG sensors were utilized.

The fiber Bragg grating (FBG) sensor is a spatial phase grating formed in the fiber core using the photosensitivity of the fiber material, as shown in Figure 3(a). These gratings form a narrow band (transmission or reflection) filter or reflector [41], as shown in Figure 3(b). The reflection spectrum of the Bragg grating depends on its bandwidth and peak reflectivity, with a functional relationship being established with parameters such as grating spacing and refractive index modulation coefficient, as shown in Formula (3). Its optical properties are sensitive to the changes of physical quantities of the external environment.

Any physical process that changes the grid pitch (such as temperature change and stress change) causes a reflected-light wavelength shift, as shown in Figure 4. The relationship between the center wavelength change and the measured physical quantity was established and calibrated as shown in Formula (4) [42–45], so that the change in the center wavelength can be measured.

$$\lambda_B = 2n_{\text{eff}} \cdot \Lambda, \tag{3}$$

$$\frac{\Delta\lambda_B}{\lambda_B} = (1 - P)\varepsilon + (\alpha + \xi)\Delta T. \tag{4}$$

Let $K_\varepsilon = \lambda_B(1 - P)$ and $K_T = \lambda_B(\alpha + \xi)$. Then Formula (4) becomes

$$\Delta\lambda_B = K_\varepsilon\varepsilon + K_T\Delta T. \tag{5}$$

In Formula (5), K_ε is the FBG strain sensing sensitivity coefficient, and K_T is the FBG temperature sensing sensitiv-
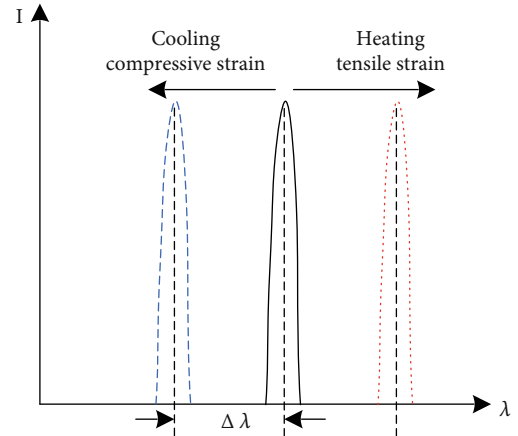

Figure 4: Wavelength changes corresponding to temperature and strain [42].

ity coefficient. For the quartz optical fiber, $P = 0.22$, $\alpha = 0.55 \times 10^{-6}/\circ C$, and $\xi = 6.67 \times 10^{-6}/\circ C$. When $\lambda_B = 1550$ nm, $K_\varepsilon = 1.2$ pm/$\mu\varepsilon$ and $K_T = 11.19$ pm/$\circ C$.

When the effect of temperature is not considered, the wavelength change of FBG only reflects the stress or strain change of the surrounding environment, meaning FBG can be used as a strain sensor. FBG is fragile, being a glass fiber, so it needs to be packaged carefully depending on the environment of its use.

3.1. Design of Fiber Grating Sensor

3.1.1. Sensor Design. The cubic similar material specimen was used as the overall similar model to simulate the accumulation of deep block rock in the model test. The space
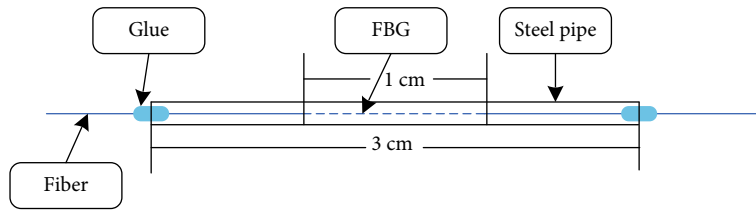
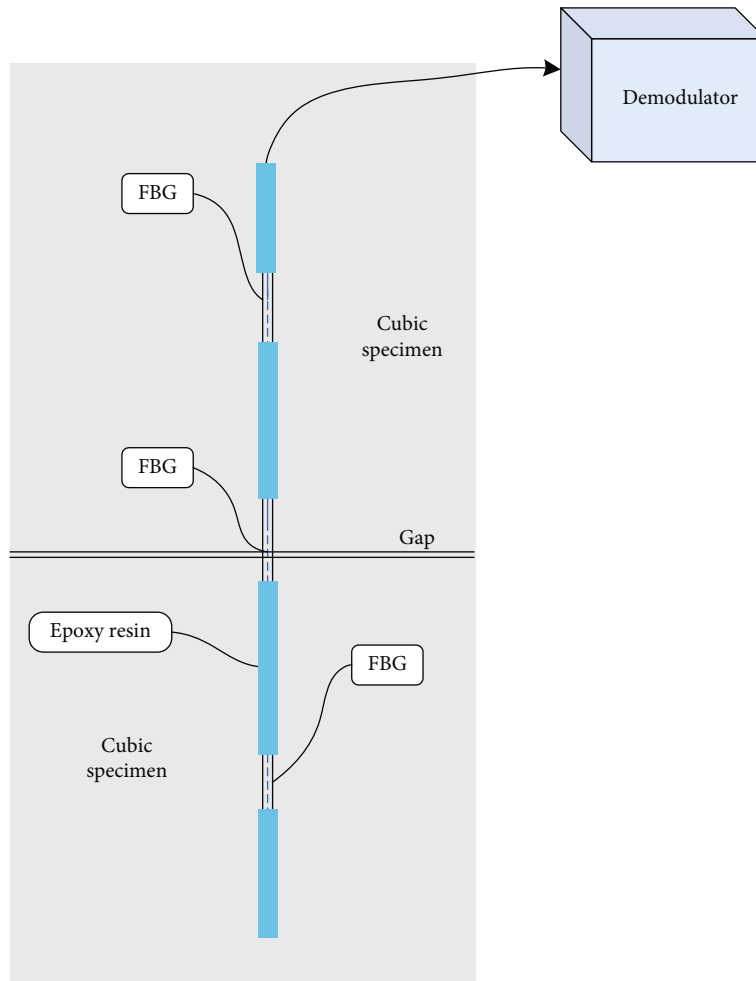FIGURE 5: Structure of a single FBG.

FIGURE 6: Vertical placement of the three-series FBGs.

between the specimens was larger than the natural space of a single small specimen, and the space would be compacted by the confining pressure. The gap between some specimens was reserved and filled with the fine sand layer. When the block was under confining pressure, there would be a fault. Thus, the geological fault of block rock was simulated. The sensor was placed along the contact interface between the specimens. A large strain would be generated as a result of the application of confining pressure, and a significant displacement would be induced in the macroscopic perspective. The range of compressive strain of bare grating is small, usually within 1000 microstrains. Therefore, the sensor has to be able to withstand the huge strain generated by confining

pressure in the early period and carry out accurate measurement subsequently.

As a bare fiber grating has a diameter of $125\,\mu$m and limited shear resistance, fiber grating was packaged before placement in the similar materials. Sensors with a large range of compressive strain and multipoint distributions were needed in the first and third periods of the test. Therefore, polyimide was applied to the grating to increase its shear resistance. Three hundred and four stainless steel capillary pipes with a diameter of 0.8 mm and a thickness of 0.2 mm were used for encapsulation. Since a single specimen of the similar material was a cube of 10 cm length, strain variation had to be measured in both the single specimen and

adjacent specimens. The length of grating area is 1 cm, the length of sensor is 3 cm, and the spacing of grating is 4 cm.

The grating was encapsulated in the steel capillary pipe for pretensioning. First, one end of the fiber was cemented with quick-drying glue to the steel capillary pipe, and then, a counterweight of 3 kg was hung on it to achieve the prepulling effect. Afterwards, the other end of the fiber was cemented with quick-drying glue to the steel capillary pipe. When the glue solidified, the grating was totally encapsulated by the pipe. The steel capillary pipe protects the grating and reduces the strain transfer rate. When load was applied to the steel pipe, the strain of the pipe tube was smaller than that of the fiber under the same load because the elastic modulus of steel is larger than that of fiber. This reduces the strain transfer and expands the measurement range of the sensor. Epoxy resin or hot melt adhesive about 1–2 mm in thickness was used to paste and fix the sensor to the specimen. Except the 1 cm length of the steel pipe where the grating area was located, all other attachments were with adhesive. Figures 5 and 6 illustrate the specific design.

3.1.2. Frequency Response.

In deep-rock model tests, the strain frequency response of the sensor must meet the frequency requirements of impact loading. High-pressure piston impact is a high-speed process, where similar materials are compacted under confining pressure in the closed device and stress wave propagates downwards within the specimen. In the current experiment, the maximum shock disturbance peak was 3 MPa, the boost time was 10–100 ms, and the positive pressure time was about 30–300 ms. In order to record the complete strain change process in shock generation, the data sampling interval of the sensor should be at least 1–2 ms, so the sampling frequency should be more than 1 kHz. In this experiment, the demodulation instrument of the grating sensor was MOI-sm 130 series with a sampling frequency of 2 kHz, which could meet the requirements of the test.

In both the tube and substrate packaging, the lag time of strain waves to FBG was of the order of 10^{-7} s [46], and the propagation speed of the strain waves in the similar materials was about 400–500 m/s. For the test model with a length of 1.3 m, the time taken was of the order of 10^{-4} s, so the propagation time of the strain waves in the adhesive layer and the encapsulation layer of the steel capillary pipe was negligible in this experiment.

3.2. Placement of the Grating Sensors.

The sensors were buried inside the specimen and glued with epoxy resin or hot melt adhesive. Since the packaging materials and adhesive layer perform differently from the fiber, the impact of packaging materials and adhesive layer on strain response and strain transfer should be considered in high-frequency measurements.

Bare fiber Bragg grating was used to measure the beam of constant strength [47–50] using adhesive (502 quick drying glue, epoxy resin). When the paste length was more than 3 cm and thickness was not more than 0.1 mm, the strain transfer rate of the strain gauges on the concrete specimen could reach 95%–96% under static loading.
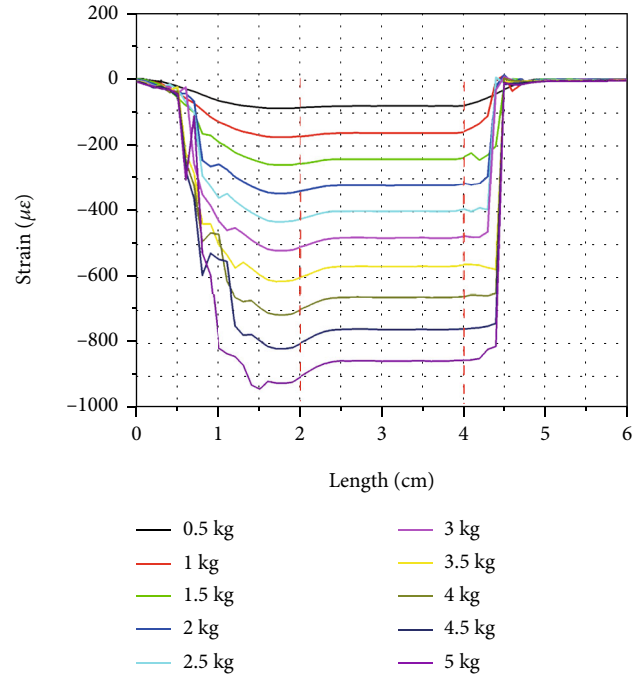

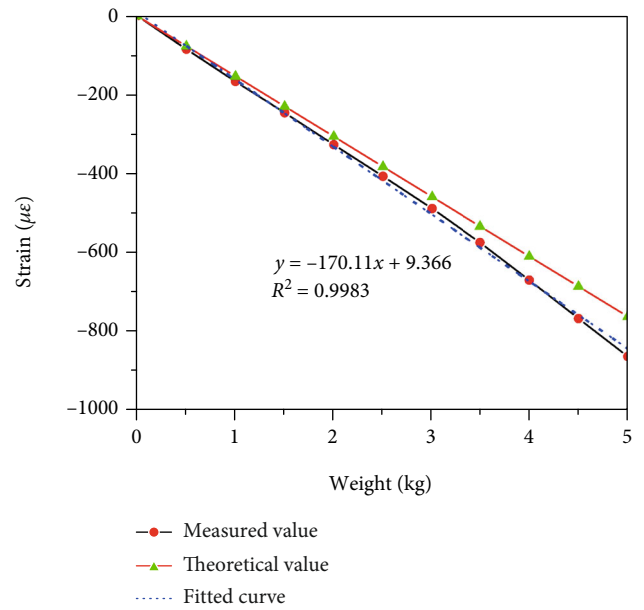Figure 7: Measured results of FBG sensor in the test on beam of constant strength.

$$y = -170.11x + 9.366$$
$$R^2 = 0.9983$$

Figure 8: Comparison between measured and theoretical values.

3.2.1. Calibration Experiment on Beam of Constant Strength.

A calibration experiment was carried out by encapsulating a 3 cm long polyimide-coated optical fiber sensor, and the encapsulated steel capillary pipe was pasted on a beam of constant strength using the quick-drying glue. The fiber sensor had a resolution of 1 mm per point. 500 g weights were loaded each time, and the total load applied was 5000 g. The results are shown in Figure 7. In this study, the strain is positive for tension and negative for compression. The measured results
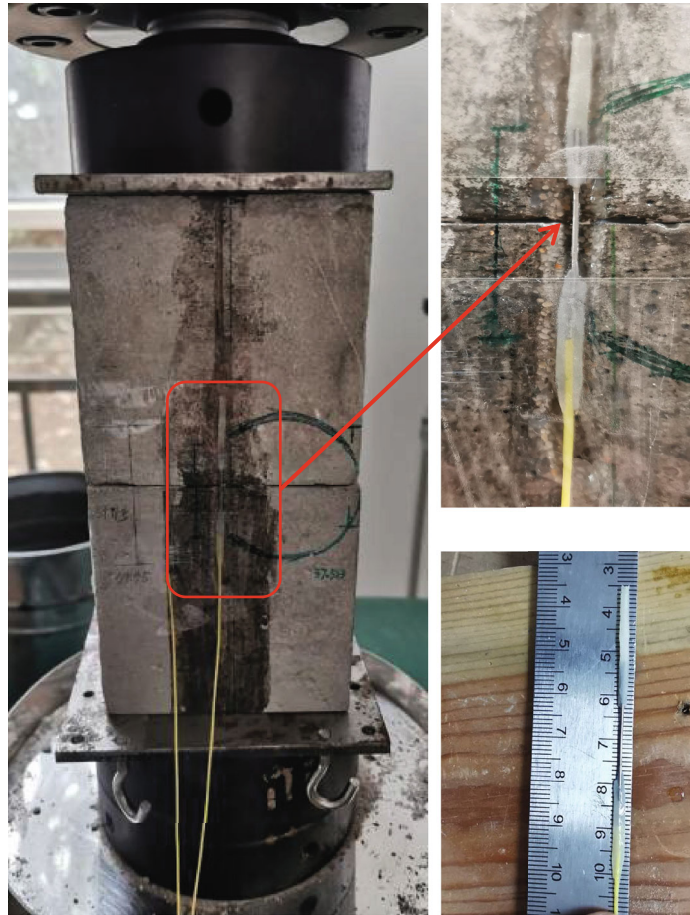
FIGURE 9: Uniaxial compression test of sensor in a cubic specimen.

showed that the deformation of the adhesive and steel pipe caused a fluctuation of about 0.5 cm at both ends within a 3 cm range in the sensor, but the area covering 2 cm in the middle exhibited stable readings. As the measurement range of the actual designed grating area was 1 cm, the average value of the strain in the range of 2–4 cm was compared with the theoretical values of strain of beam of constant strength, with results illustrated in Figure 7.

As Figure 8 illustrates, the linear fitting of measured strain reveals that R^2 exceeds 0.99, indicating good linearity. The measured and theoretical values varied slightly because of the thicknesses of the adhesive layer and steel pipe. The strain measured by the sensor was slightly larger than the theoretical strain of the beam of constant strength. In the model tests, the length of the steel capillary pipe in the sensor was 3 cm and the length of grating region was 1 cm in the middle. Hence, no large strain due to deflection was induced. The calibration experiment confirms that the sensor design and pasting method can effectively measure the actual strain.

3.2.2. Applicability in Cubic Specimen. As illustrated in Figure 9, the processed single grating sensor was cemented to the joint between the two cubic specimens by encapsulation and pasting, as reported elsewhere. The specimen was a 10 cm cube intended to test whether the strain range and variation of
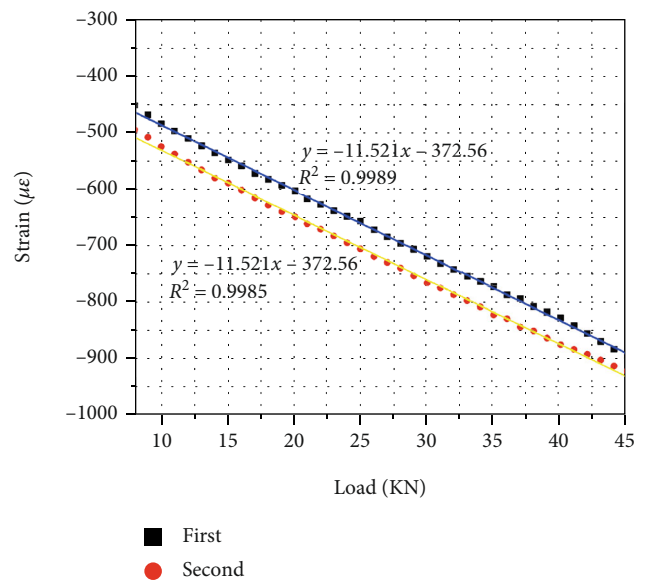

FIGURE 10: Linear fitting of compressive strain and load.
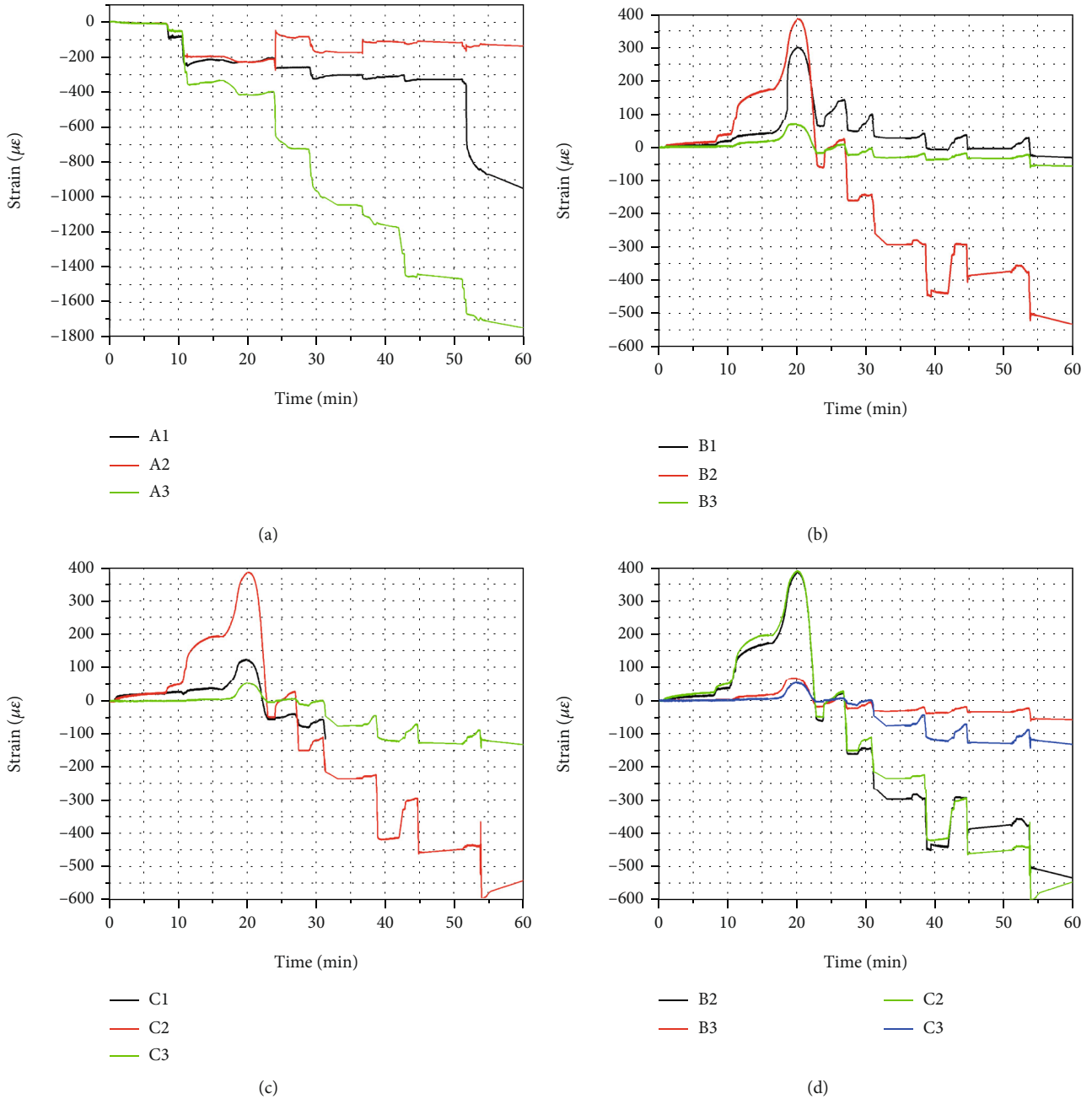
(a)

(b)

(c)

(d)

FIGURE 11: Strains measured by sensors during the loading of confining pressure: (a) vertical A; (b) horizontal B; (c) horizontal C; (d) strains of B and C.

the sensor could be accurate in the environments where it is required, through uniaxial compression tests.

A uniaxial compression test was carried out with two loads by force control. The loading rate was 0.02 mm/s, and a small MTS testing machine was used in the experiment. The preloading test was carried out before the test, during which the peak loading force was 40 kN. The peak loading force increased to 45 kN during the loading test.

In the uniaxial compression test, the void compaction of the specimen was dominant at the initial stage of loading, after which the elastic deformation became dominant where stress

was linearly related to the strain. Data between 8 kN and 45 kN were selected for linear fitting analysis; the results are shown in Figure 10. Since the capillary pipe is made of steel and the temperature remained unchanged during loading, the specimen support function and temperature influence of steel pipe are ignored in the analysis. As shown in Figure 10, the R^2 of the two test results are both above 0.99 with the same slope, suggesting good linear fitting between the strain testing data and loading data as well as good repeatability of sensor readings. In summary, this kind of sensor can effectively measure the compressive strain at joints of the cubic
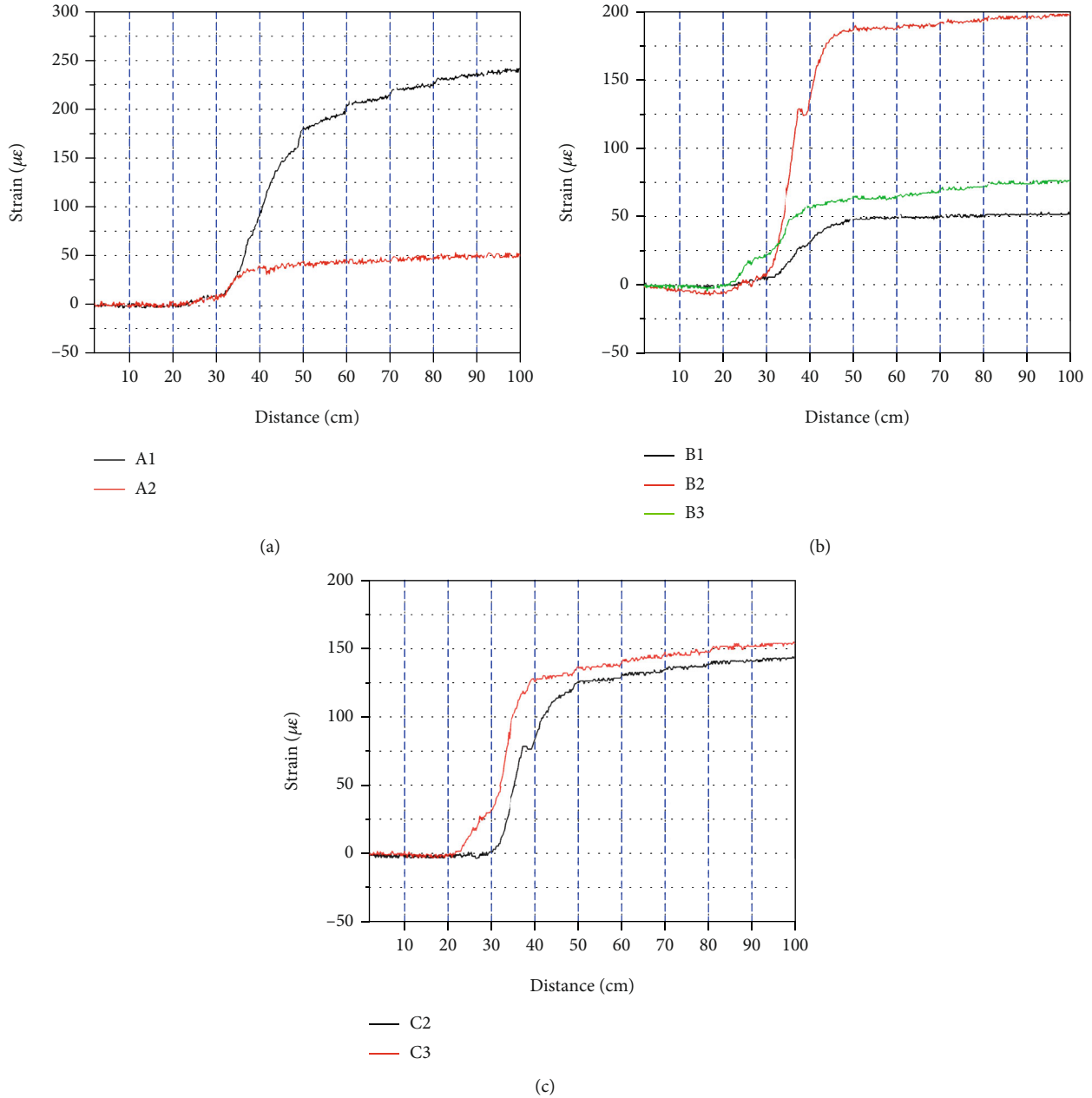
(a)

(b)

(c)

Figure 12: Strain monitoring during excavation: (a) monitored data of grating string A; (b) monitored data of grating string B; (c) monitored data of grating string C.

specimens. Experimental results demonstrated the viability and applicability of such designs. Therefore, the model test on large-scale specimens was carried out using this measurement method.

4. Results and Discussion of Model Tests

4.1. Static Loading. Confining pressure was loaded in the following sequence: top-front and back-left and back-right; then, the single-stress loading gradient was controlled to be about 0.1 MPa. The overpressure required to be loaded was 0.5 MPa, sufficient to cause the creep of the specimen to accelerate to the initial high crustal stress state. Due to the

rapid pressure reduction caused by the deformation of the specimen at the early stage of the test, the loading was applied six times. After stabilizing the pressure for two days, the pressure in all three directions was reduced to 0.16 MPa to simulate the stress environment at a depth of 300 m. The next stage of the test was carried out when the internal stress of the specimen was stable. Figure 11 illustrates strain measurements when the confining pressure was increased to 0.5 MPa. As observed, as the confining pressure increased, load was gradually transferred to the interior of the specimen, and the strains of grating A2, B1, B3, C1, and C3 which were cemented to the block became gradually closer. Despite the similarity in the trends of A1 and A3 at the joint, the

uniform deformation was different between the blocks. The stress during loading at D3 was larger than that at D2 upon completion of loading, which was consistent with their strain responses. The strain measured by transverse grating string B2 was much greater than those of strings B1 and B3 inside the specimen, suggesting that the deformation between blocks was significantly larger than the deformation inside the block during loading. Compared with B3, B1 was closer to the specimen boundary or loading interface, so the measured strain of B1 was greater than that of B3. However, with increasing confining pressure, the strain was gradually transferred to the interior. After the loading process was completed, B3 was close to B1. Figure 11(d) shows the measured data of the transverse grating series. B and C, B2 and C2, and B3 and C3 were located in the same working positions, and their strain variation trends and values were basically the same, demonstrating that strain could be measured through the epoxy resin and hot melt adhesive during loading. Since the wavelength measurement range of C1 grating was about 1020 nm, its strain range exceeded the range of the demodulation instrument after compression, so it failed. Therefore, it is better for the wavelength of the grating in subsequent experiments to be 5 nm more than the recognizable minimum wavelength of the interrogation instrument, namely, 1025 nm.

4.2. Strain Testing during Simulated Excavation. The simulation of cavern excavation commenced when the internal pressure of the specimen stabilized at 0.16 MPa. The excavation was carried out automatically with a drill. The excavation hole was circular with a diameter of 20 cm. The drilling advance rate was 1 cm/min, and each single excavation length was 10 cm. The excavation was halted for 10 min every 10 cm, and the excavated cavern was 100 cm in depth and completed in 10 rounds of excavation. Strains during excavation are presented in Figure 12. The vertical dotted line indicates the starting point of excavation. The distance of the grating layout section to the front elevation was 40 cm. Therefore, when the fourth of excavation was completed, it would be close to the section where the sensor was located. The fifth round of excavation (40–50 cm) was therefore conducted in the specimen with the glued grating sensor. So as not to clutter the diagram, the figure only presents strain changes during excavation while the strain measurement during the rest periods is omitted.

The data obtained shows the grating string sensor could effectively detect strain changes at multiple points, and strain changes reflected the internal stress state of the specimen. During excavation, the force acting on the radial direction of the cavern gradually changed from stress to tension, suggesting an inward shrinkage of the cavern along the radial direction. At an excavation depth of 25 cm, the grating sensor started to respond when the distance from sensor was 15 cm, demonstrating that appropriate placement of strain monitoring sites could be used for early warning. Even when the deformations that occurred in the cavern were minor, the sensor could respond quickly for timely decision-making.

The gratings arranged on the specimen changed the most during the excavation process near the section where
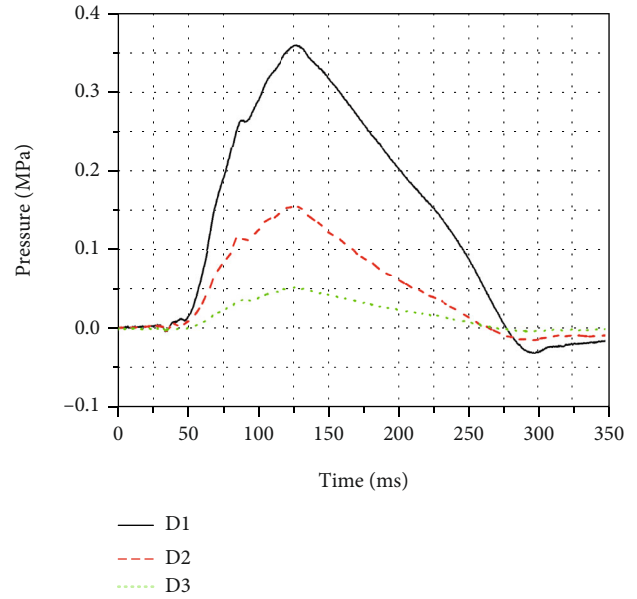

Figure 13: First shock pressure waveform.

the sensor was located, and when the pasted test block was excavated (40–50 cm), the change tended to be gradual. However, the sensor at the joint still had a large strain change when a block between 40 and 50 cm was excavated. The vertical A1 measurement data showed that when the excavation reached a depth of 70 cm, the strain variation gradually decreased but still presented the trend of a gradual growth. According to the monitoring data, when it was close to the excavation section, the surrounding rock moved to the interior of the cavern as a whole, causing the radial relaxation. During excavation, a single block moved to the interior of the cavern, but the movement was not perceptible. The results demonstrate that a crack in the rock poses a great risk to construction safety. In addition to the timely support of the construction at the surface of underground engineered structures, construction safety monitoring is a necessary measure to avoid hidden dangers; deformation of the top and middle sections of the cavern should be continuously monitored to ensure safety. According to the monitoring results, tunnel excavation is not just a simple plane problem, so a triaxial model test can be performed to accurately investigate the change in cave strain during excavation. Additionally, the quasidistributed strain monitoring using FBG sensors can be conducted for the purpose of early warning, construction monitoring, and long-term monitoring in deep rock engineering. The sudden change of strain data in Figure 12(b) is due to the intermittent acquisition process, which leads to the discontinuity of some strain data. But it had no effect on the test results.

4.3. Strain Testing during Shock Generation

4.3.1. Pressure Curve and Grating Curve. Several shock tests on multiple specimens were conducted to further investigate the monitoring performance of the grating sensor and cavern damage under shock. The test results in the first shock
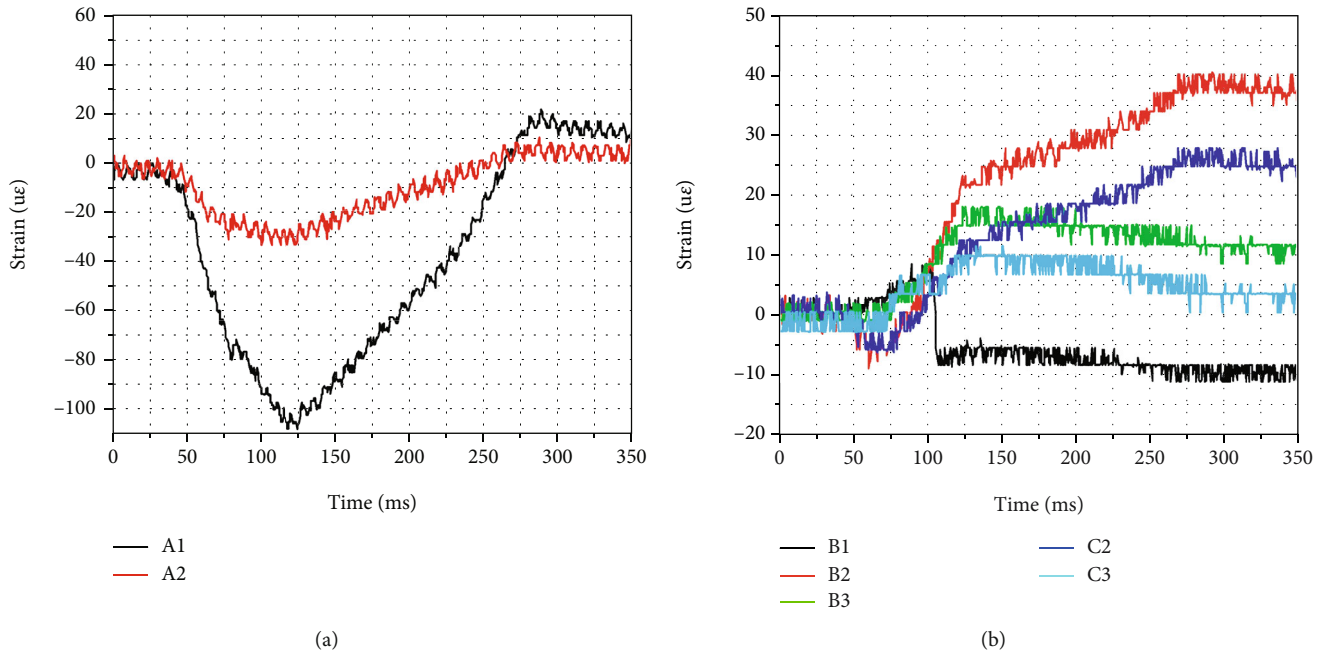
(a)

(b)

FIGURE 14: Monitored strain during first shock: (a) vertical grating string; (b) transverse grating string.

test were selected for detailed description of the performance of the grating sensor.

Figure 13 illustrates the monitored pressure sensor during the first shock. Here, D1 was placed on the top of the specimen at a depth of 5 cm, and the shock pressure monitored by D1 was used as the shock pressure in the test. In the first test, shock pressure peak was 0.36 MPa. As shown in Figure 13, the peak shock pressure at the depths of 40 and 50 cm were 0.15 and 0.05 MPa, respectively. With increasing depth, peak shock pressure gradually declined. This can be attributed to pressure decay during propagation. Further, the surrounding rock exhibited loosening after excavation, resulting in accelerated pressure decay. In summary, the strategy of excavation before shock generation could simulate the impact of loosening of surrounding rock on shock after excavation, thus becoming capable of modeling the field test condition more accurately.

According to the pressure curve and monitored data of grating string A shown in Figures 13 and 14, respectively, both waveforms are basically the same. Under shock, the grating strain sensor could fully monitor the change in strain. The results demonstrated that the fiber grating sensor as well as the frequency of monitoring means met the requirements, indicating good applicability of grating sensors in shock tests.

According to strain monitoring results, vertical grating string A experienced compressive strain initially but tensile strain later under the effects of ground-shock disturbance. This is because the shock force was a compressive force, resulting in the vertical compression above the cavern. Upon completion of shock generation, there was a slight movement of the block toward the cavern interior, showing the tendency of strain to be tensile. The tension was barely per-

ceptible due to the relatively small shock force. However, significant tensile strains were monitored by transverse grating strings B and C. Depending on when the shock stress and transverse strain occurred, the left and right sides of the cavern were subjected to tension horizontally under shock, suggesting that the left and right sides of cavern moved inward in response to shock. Hence, it can be concluded that when shock propagated from top to bottom, the left and right sides of cavern showed more severe deformation than the top and bottom. Additionally, the strain changes in the load-increase stage were more drastic and increased faster than those in the load-decrease stage under shock, indicating that the deformation of the cavern during loading was more severe than that during unloading. The deformation during unloading still continued but became less severe.

The strain differences between B2/C2 and between B3/C3 show that pressure changes at the same position were basically the same, suggesting that either pasting method could be used for strain measurement in the model; the methods verified each other, demonstrating high accuracy of the experimental results. Due to the first impact test, the impact pressure is small, and the maximum strain generated is only more than $100 \, \mu\varepsilon$, so the small vibration changes in the strain test data can be clearly seen.

4.3.2. Grating Variation under Different Shock Pressures. After examining the cave strains and cavern damage under different pressures, this study accepted the other two test results. The three tests were different only in shock pressure while other conditions were all the same. The top shock pressure peaks of the second and third specimens were 0.9 and 2.0 MPa. The monitored strains are given in Figures 15 and 16.
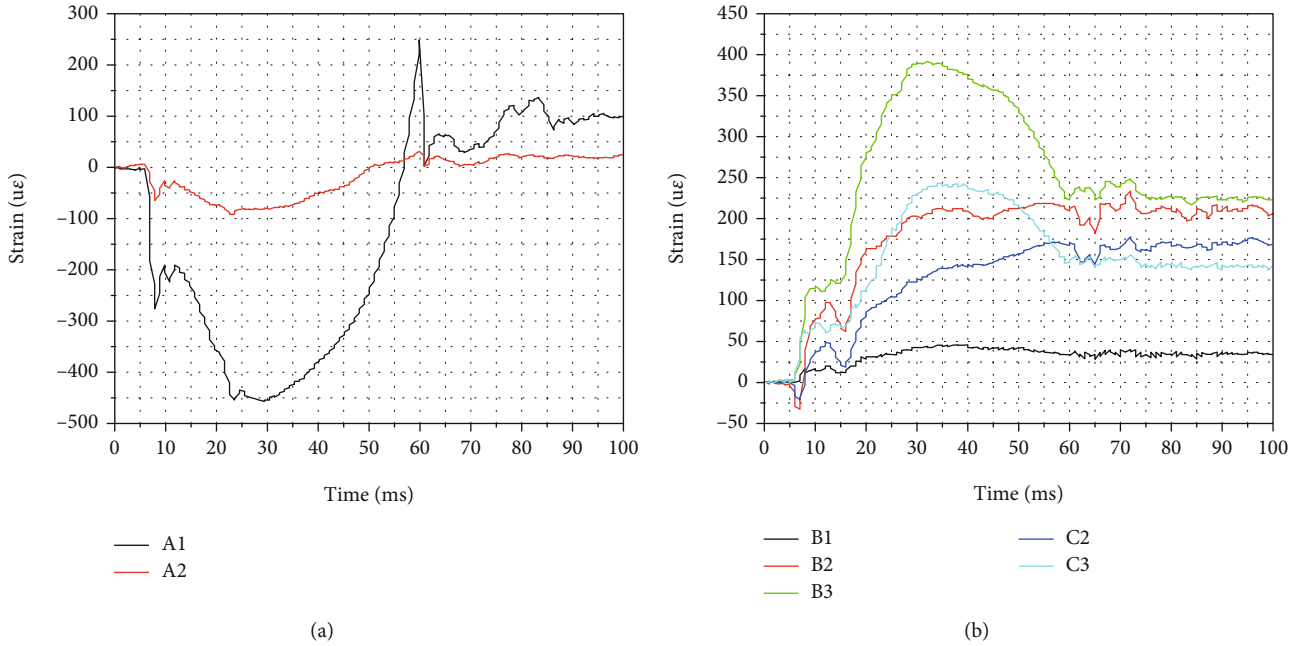
(a)

(b)

FIGURE 15: Monitored strains in the second shock: (a) vertical grating string; (b) transverse grating string.
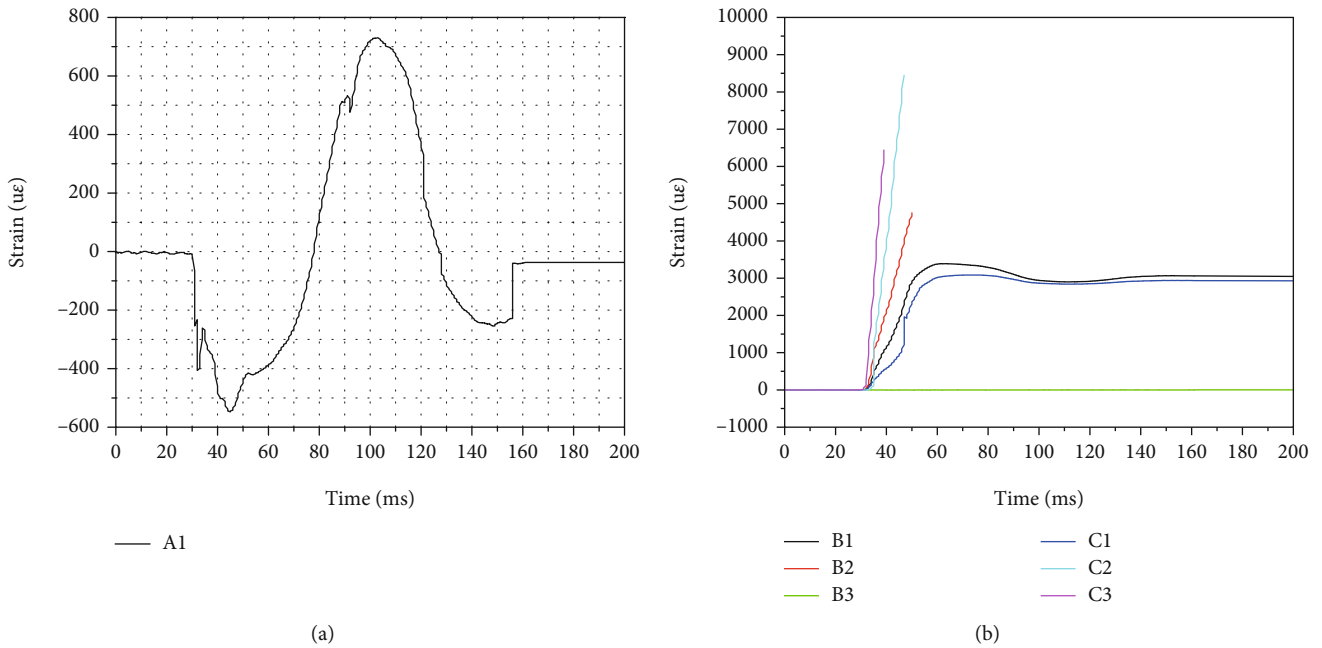

(a)

(b)

FIGURE 16: Monitored strains in the third shock: (a) vertical grating string; (b) transverse grating string.

Three shocks were applied to the model, with the results indicating that the larger the shock pressure was, the greater the top peak compressive strain during shock generation and the more significant the tensile strain. The maximum tensile strains at site A1 in the three shocks were $20\,\mu\varepsilon$, $250\,\mu\varepsilon$, and $710\,\mu\varepsilon$, respectively. Additionally, the monitored horizontal strain of the right side of the cavern clearly showed that the inward compression of cavern was proportional to the shock pressure. As the shock pressure grew, the maximum

tensile strain grew astronomically, seriously threatening the cavern.

According to the monitored data of grating string A sensors placed in the block joint and block surface, the strain at the joint was significantly larger than the strain on the block surface. In the first two shocks, the strain peaks at A1 were 3.5 and 4.5 times higher than those at A2. The results demonstrated that the block movement was more severe along the shock direction, indicating more attention should be
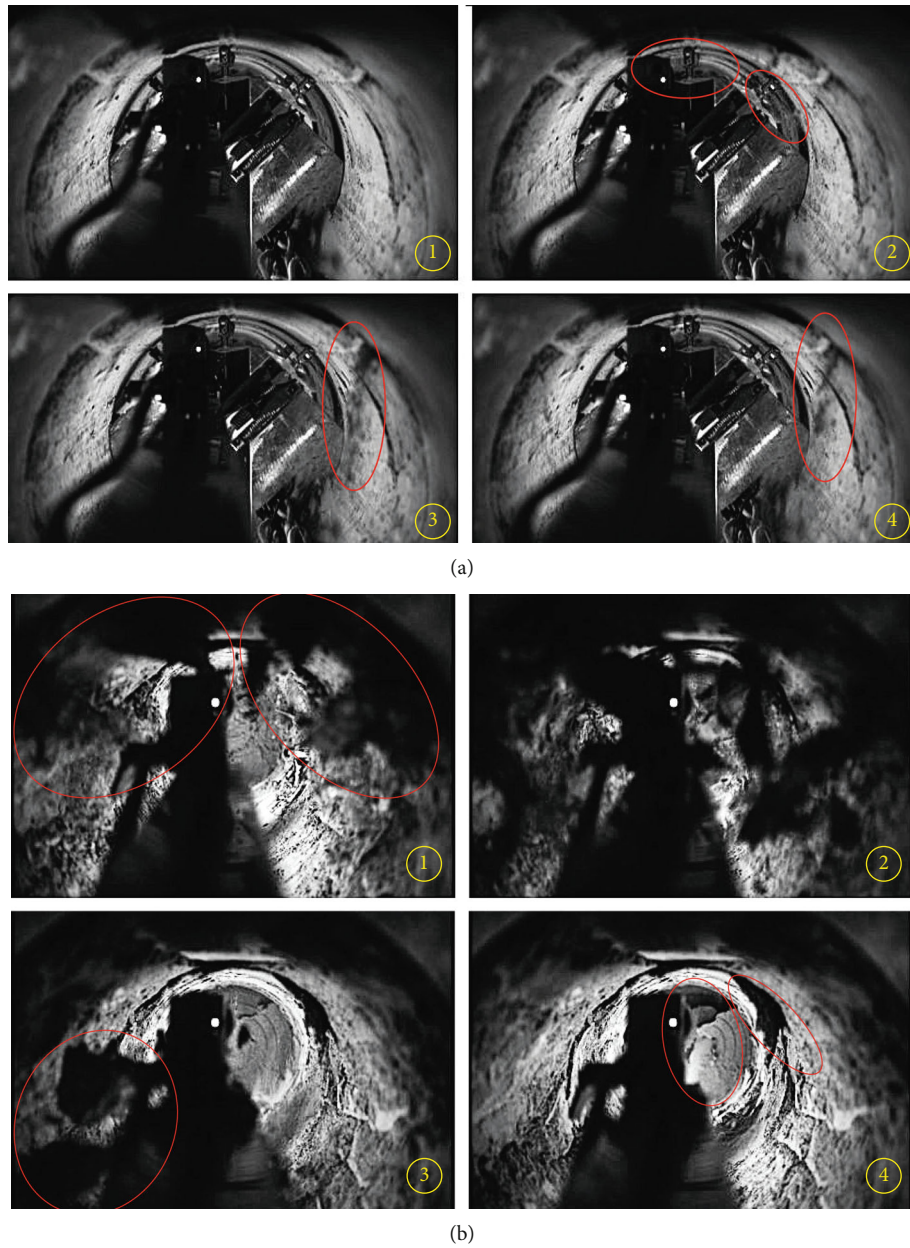
(a)

(b)

FIGURE 17: Damage monitoring under shock in: (a) the second shock; (b) the third shock.

paid to the block characteristics of rock. In the third shock, site A1 was first subjected to compression and then tension, after which it was in a static state, suggesting the up-and-down flipping of the block, thus the presence of a pendulum wave. However, the monitored data of grating strings B and C showed that, when the shock force was relatively small, block movement dominated the right side of the cavern, whereas when the shock force was relatively large, failure due to lost strength was dominant, suggesting that dynamic stress concentration occurred at both sides of the cavern under shock. When subjected to the third shock, due to the excessively large shock pressure, dynamic stress concentration occurred at the right side of the cavern, and tensile strains at sites C1 and C2, which were 15 cm away from

the wall, reached 3000 $\mu\varepsilon$ and did not recover after the shock was completed, indicating significant plastic strain, while strains in other sites exceeded the monitoring range of the sensor.

In summary, the use of continuous medium mechanics to describe the mechanical behavior of block rock under shock disturbance has certain limitations, and the block characteristics of rock should be fully taken into account when deep caverns are subjected to ground shock.

4.3.3. Monitored Strain and Damage. Figure 17 illustrates cavern damage during shock generation. There are four images arranged chronologically. After the first shock, the cavern was not damaged and no image has been presented. During second

shock, the cavern was damaged. As illustrated in Figure 17(a) (2), particle ejection occurred first in the block, and the damage occurred in the vault and spandrel but was not severe. Then, projectiles of particles appeared at the spandrel of the intact part. Overall, the failure was not severe, particle size was relatively small, and the cavern was only slightly damaged. During the third shock, the damage mainly occurred at the sides and the spandrel. As depicted in Figure 17(b) (1), block ejection occurred. With the continuous effect of the shock pressure, ejected blocks kept increasing in quantity and size. As Figure 17(b) (2) shows, the ejected blocks filled up the entire window, the blocks being significantly larger than those expelled by the second shock. Figure 17(b) (3) shows that after other blocks fell on the ground, new blocks continued to eject outside for a long period. As shown in Figure 17(b) (4), after the shocks had stopped, blocks continued to fall because of plate crack; they gradually fell off, and large blocks were found collapsed from the working face of the cavern.

Based on the examination of monitored strains and cavern damage, the mechanism of failure can be explained. In all three shocks, when the shock force was relatively large, both sides of the cavern were under tension, indicating that the inward movement of the left and right sides of the cavern under shock and the inward shift was proportional to the shock. In the third shock, strains of the strain gauge 5 cm away from the cavern and the strain gauge cemented to the block joint were all beyond the monitoring range, suggesting that severe inward deformation occurred at these two places; the strain at locations 15 cm away from the side wall of the cavern reached 3000 $\mu\varepsilon$, suggesting the occurrence of significant plastic deformation. In summary, rockburst usually took place in the left and right sides of the cavern because the presence of stress concentration led to cavern deformation, causing the surrounding rock on the both sides of the cavern to cave in. When the strain exceeded the threshold, tension failure would occur, inducing the release of elastic energy stored in rock. The experimental results explained the causes of rockburst and the mechanism of the V-shaped crater to a certain extent. The experimental results demonstrate good applicability and high accuracy of grating sensors in model tests.

5. Conclusions

Using a customized set-up for the simulation of the ground shock effect on deep cavern, this study carried out simulations that included crustal stress loading, cavern excavation, and ground-shock disturbance using a 1.3 m cubic specimen. The proposed FBG sensor was modified to test for strain monitoring. The following conclusions can be drawn:

(1) In internal strains of specimens under cavern loading, excavation and shocking were measured using the customized FBG strain sensor. With the sensor validation test and model test, this study proved the applicability and viability of FBG sensors. The strain

testing results provided important data for the analysis of the degradation mechanism of caverns

(2) The changing roles of stress and strain of cavern surrounding rock during excavation were obtained in the model test, and it was proved that excavation before shocks in the test could simulate the loosening of surrounding rock and the impact of loosening surrounding rock after being subject to shocks. Therefore, it can be concluded that the test manner of excavation before shock generation can adequately simulate field conditions

(3) The monitored strain indicated that under the impact of the top plane wave, there would be a significant tensile strain on the left and right sides of the cavern, which was why the damage was mainly on both sides of the cavern under impact, thus revealing the mechanism of V-shaped craters on both sides of cavern to a certain extent

(4) The simulation adequately captured failure phenomena of deep tunnels such as particle ejection, block collapse, plate cracks, and face collapse; in addition, the pendulum traveling wave was successfully monitored by the FBG sensor

Data Availability

The data used to support the findings of this study were supplied by Nanjing University of Science and Technology under license and so cannot be made freely available. Requests for access to these data should be made to Zhihao Li (17865191593@163.com).

Conflicts of Interest

The authors declare that they have no conflicts of interest.

Acknowledgments

References

[1] H. Manchao and Q. Qihu, *The Basis of Deep Rock Mechanics*, China Science Publishing & Media Ltd, Beijing, 2010.

[2] E. Fumagalli, *Statical and Geomechanical Model*, Springer, New York, 1973.

[3] C. Xinghua, *Brittle Material Model Test of Structures*, China Water& Power Press, Beijing, 1979.

[4] S. Tai, "Development of geomechanic model experiment techniques," *Journal of Yangtze River Scientific Research Institute*, vol. 18, no. 5, pp. 32–34, 2001.

[5] C. Anmin, G. Jincai, and S. Jun, "Application study on the geomechanical model experiment techniques," *Chinese Journal of Rock Mechanics and Engineering*, vol. 23, no. 22, pp. 3785–3789, 2004.

[6] D. Yingji, "Research status and development trend of geomechanics model test," *Water Resources & Water Engineering*, vol. 2, pp. 64–67, 1996.

[7] Y. Wenzhong, *Similarity Theory and Static Model Test*, Xi'an Jiaotong University Press, Xi'an, 1998.

[8] R. E. Heuer and A. J. Hendron, *Geomechanical Model Study of the Behavior of Underground Openings in Rock Subjected to Static Loads (Report 2)-Tests on Unlined Openings in Intact Rock*, AD Report, 1971.

[9] A. J. Hendron, P. Engeling, and A. K. Aiyer, *Geomechanical Model Study of the Behavior of Underground Openings in Rock Subjected to Static Loads (Report 3)-Tests on Lined Openings in Jointed and Intact Rock*, AD Report, 1972.

[10] E. Fumagalli, "Geomechanical models of dam foundations," in *In: Proceedings of the International Colloquium on Physical Geomechanical Models*, Bergamo, Italy: ISRM, 1979.

[11] L. Mueller, G. Reik, E. Fecker, and B. Sharma, "Importance of model studies on geomechanies," in *In: Proceedings of the Intemational Conference on Geomechanical Model*, Bergamo, Italy: ISRM, 1979.

[12] N. R. Barton, "A low strength material for simulation of the mechanical properties of intact rock mechanics models," in *In: Proeeedings of the International Society of Rock Mechanics*, pp. 99–110, Belgrade, Yugoslavia: ISRM, 1970.

[13] W. Hanpeng, L. Shucai, Z. Xuefen, and Z. Weishen, "Research progress of geomechanical model test with new technology and its engineering application," *Chinese Journal of Rock Mechanics and Engineering*, vol. 28, pp. 2765–2772, 2009.

[14] A. Mendez, T. F. Morse, and F. Mendez, "Applications of embedded optical fiber sensors in reinforced concrete buildings and structures," *OE/FIBERS'89. International Society for Optics and Photonics.*, pp. 60–69, 1990.

[15] C. H. A. I. Jing, Y. U. A. N. Qiang, and L. I. Yi, "Application analysis on method of physical model test with optical fiber sensing technique," *Journal of Engineering Geology*, vol. 23, no. 6, pp. 1100–1109, 2015.

[16] M. Iten and A. M. Puzrin, "Monitoring of stress distribution along a ground anchor using BOTDA," in *Sensors and Smart Structures Technologies for Civil, Mechanical, and Aerospace Systems 2010*, 2010.

[17] A. Klar and R. Linker, "Feasibility study of automated detection of tunnel excavation by Brillouin optical time domain reflectometry," *Tunnelling and Underground Space Technology*, vol. 25, no. 5, pp. 575–586, 2010.

[18] H. Sanada, Y. Sugita, and Y. Kashiwai, "Development of a multi-interval displacement sensor using fiber Bragg grating technology," *International Journal of Rock Mechanics and Mining Sciences*, vol. 54, pp. 27–36, 2012.

[19] J. Frieden, J. Cugnoni, J. Botsis, T. Gmür, and D. Ćorić, "High-speed internal strain measurements in composite structures under dynamic load using embedded FBG sensors," *Composite Structures*, vol. 92, no. 8, pp. 1905–1912, 2010.

[20] S. Nan and Q. Gao, "Application of distributed optical fiber sensor technology based on BOTDR in similar model test of backfill mining," *Procedia Earth and Planetary Science*, vol. 2, pp. 34–39, 2011.

[21] H. Zhu, S. Bin, and Z. Chengcheng, "Current progress and trends in opto-electronic sensor-based monitoring in geo-engineering-a summary of 6th OSMG-2017," *Journal of Engineering Geology*, vol. 28, no. 1, pp. 178–188, 2017.

[22] L. Haowu, "Optical fiber sensor network for crack monitoring in concrete gravity dams," *SHUILI XUEBAO*, vol. 10, pp. 61–64, 1999.

[23] J. Shanchao, C. Yuqiang, and S. Qingmei, "Research on the micro and high-precision fiber Bragg grating soil pressure sensor," *CHINESE JOURNAL OF LASERS*, vol. 40, no. 4, p. 0405002, 2013.

[24] W. Jun-jie, J. De-sheng, and L. Angyu-Fei, "A differential optical fiber grating pressure cell and the temperature characteristic," *Journal of Optoelectronics Laser*, vol. 18, no. 4, pp. 389–392, 2007.

[25] C. Fu-yun, L. Chuan, and C. Er-kuo, "Dual-diaphragm fiber Bragg grating soil pressure sensor," *Rock and Soil Mechanics*, vol. 34, no. 11, pp. 3340–3345, 2013.

[26] L. Zhong-Kui and W. Ai-Min, "Application and consideration of using fiber-sensor measurement in a 3D geo- mechanical model test," *Experimental Technology and Management*, vol. 23, no. 12, pp. 62–65, 2006.

[27] Y. Geng-xin, Z. Lin, and Z. Hong-hu, "Application of fiber Bragg grating sensor in geomechanical model test of arch dam," *Journal of Yangtze River Scientific Research Institute*, vol. 29, no. 8, pp. 52–57, 2012.

[28] W. Zu-tang, C. Zhi-jun, Z. Hong, and H. Xiao-fei, "Study on application and principle of strain measurement based on fiber Bragg grating sensor in material model experiment," *Machine Design and Research*, vol. 28, no. 1, pp. 82–85, 2012.

[29] W. Jing, S. Bin, and Y. Junfan, "Model test of landslides catastrophe based on fiber Bragg grating sensors," *Journal of Engineering Geology*, vol. 20, pp. 810–816, 2012.

[30] W. Jing, *Research on Multi Parameter Sensing Theory and Technology of Optical Grain Grating and Its Application in Underground Engineering Disaster Monitoring*, Shandong University, Shandong, 2011.

[31] W. Jing, L. Shu-cai, and S. Qing-mei, "Study of FBG strain sensors based on similar materiel in zonal disintegration model test," *Journal of China Coal Society*, vol. 37, no. 9, pp. 1570–1576, 2012.

[32] W. Jing, L. Shucai, and S. Bin, "Trifarious FBG sensor strain transfer characteristics and its application to tunnel excavation model test," *Journal of Engineering Geology*, vol. 21, no. 2, pp. 182–190, 2013.

[33] Z. You, Y. Wang, Y. Sun, Q. Zhang, Z. Zhang, and X. Huang, "Constitutive relation measurement of geological mechanics similar material based on fiber Bragg grating," *Optical Engineering*, vol. 56, no. 2, article 024105, 2017.

[34] S. Yang-yang, W. Yuan, and Z. Qing-hua, "Strain transfer of internal strain of model similar materials with optical fibre measurement," *Rock and Soil Mechanics*, vol. 39, no. 2, pp. 759–764, 2018.

[35] Z. Peng, S. Yangyang, Y. Zewei, and Z. Zhenglin, "Experimental study on embedded model of FBG-similar material sensor," *Piezoelectrics& Acoustooptics*, vol. 1, pp. 46–48, 2019.

[36] G. Chunsheng and Y. Jun, "Model test of overlying rock failure based on fiber Bragg grating sensing technology," *Coal Technology*, vol. 3, pp. 84–86, 2016.

[37] W. Yong-hong, Z. Ming-yi, and L. Xue-ying, "Research on comparison of fiber Bragg grating and static resistance used in Jacked model pipe pile test," *Journal of Optoelectronics·Laser*, vol. 30, no. 10, pp. 73–79, 2019.

[38] Z. Dean and C. Zhimin, "Statistical analysis of distribution law of geostress field in China," *Chinese Journal of Rock Mechanics and Engineering*, vol. 26, no. 6, pp. 1266–1272, 2007.

[39] Q. I. A. O. Dengjiang, *An Introduction to the Phenomenology of Underground Nuclear Explosions*, National Defence Industry Press, Beijing, 2002.

[40] L. Jie, W. Derong, and L. Zhihao, "Theoretical and experimental study on ground impact damage effect under large equivalent explosion. Part II: development of a simulation test system for ground impact effect of deep buried caverns," *Chinese Journal of Rock Mechanics and Engineering*, vol. 41, no. 8, pp. 1536–1551, 2022.

[41] L. Sun, *Analysis of Problems in Application of Fiber Bragg Grating Sensing Technology*, Science Press, Beijing, 2012.

[42] L. Gao, Q. Zhang, E. Li et al., "Strain monitoring of combustible gas implosion test based on fiber Bragg grating," *Shock and Vibration*, vol. 2019, Article ID 9858125, 17 pages, 2019.

[43] Y. Liao, *Fiber Optics: 1-5, 199-205*, Tsinghua University Press, Beijing, 2000.

[44] P. Ferraro and G. De Natale, "On the possible use of optical fiber Bragg gratings as strain sensors for geodynamical monitoring," *Optics and Lasers in Engineering*, vol. 37, no. 2-3, pp. 115–130, 2002.

[45] W. W. Morey, G. Meltz, and W. H. Glenn, "Fiber optic Bragg grating sensors," *SPIE*, vol. 1169, pp. 98–107, 1989.

[46] S. Li, L. Hongnan, T. Zhu, R. Liang, and R. Dong, "Dynamic characteristic and application range of FBG strain sensor," *Journal for vibration and Shock*, vol. 25, no. 3, pp. 29–34, 2006.

[47] Z. Zhenglin, W. Yuan, S. Yangyang, and Z. Qinghua, "Influence of adhesive on surface-bonded FBG sensor strain transfer coefficient," *Acta Materiae Compositae Sinica*, vol. 11, pp. 2537–2542, 2016.

[48] Y. Sun, J. Liu, Y. Wang et al., "Principles and application of polyimide fiber Bragg gratings for surface strain measurement," *Applied sciences*, vol. 7, no. 10, p. 995, 2017.

[49] S. Yangyang, W. Yuan, and Z. Zhenglin, "Analysis and experimental research on the principle of surface bonded FBG strain transfer," *Journal of Functional Materials*, vol. 7, 2016.

[50] S. Li, *Analysis of Fiber Grating Sensing Application*, China Science Publishing& Media Ltd, Beijing, 2012.